minerals

MDPI

Review

Geochemistry as a Clue for Paleoweathering and Provenance of Southern Apennines Shales (Italy): A Review

Roberto Buccione *, Giovanna Rizzo and Giovanni Mongelli

Department of Sciences, University of Basilicata, 85100 Potenza, Italy; giovanna.rizzo@unibas.it (G.R.); giovanni.mongelli@unibas.it (G.M.)
* Correspondence: roberto.buccione@unibas.it

Abstract: The southern Apennines (Italy) chain is a fold-and-thrust belt mainly derived from the deformation of the African–Apulian passive margin where shallow-water, basinal, and shelf-margin facies successions, including fine-grained sediments, occur. Here, we provide a review of the geochemistry of Meso–Cenozoic shales from the Lagonegro basin to elucidate provenance and paleoweathering. The different suites of these shales are dominated by 2:1 clay minerals and are Fe shales and shales. An R-mode factor analysis suggests Ti, Al, and LREE (F1) and K_2O-MgO (F2) covariance, likely related to the illite → smectite → kaolinite evolution during weathering. HREE and Y are distributed by phosphate minerals, suggesting LREE/HREE fractionation. The CIA paleoweathering proxy rules out non-steady-state weathering conditions and indicates that the source area was affected by moderate to intense weathering. The paleoprecipitation values derived from the CIA-K and CALMAG indices show median values in the 1214–1610 mm/y range. The Eu/Eu*, Sm/Nd, and Ti/Al provenance ratios point toward a UCC-like source excluding any mafic supply and suggest that the Lagonegro basin was connected, through a southern area, with the African cratonic area. However, the Eu/Eu* median value of the southern Apennine shales is quite similar to the value of the Archean shales, possibly indicating a less differentiated component. This is consistent, in many samples, with the value of the $(Gd/Yb)_{ch}$ ratio, suggesting that the shales likely incorporated ancient sediments derived from African Archean terranes through a cannibalistic process.

Keywords: geochemistry; Apennine shales; trace elements; rare earth elements; factor analysis; paleoclimate

Citation: Buccione, R.; Rizzo, G.; Mongelli, G. Geochemistry as a Clue for Paleoweathering and Provenance of Southern Apennines Shales (Italy): A Review. *Minerals* **2023**, *13*, 994. https://doi.org/10.3390/min13080994

Academic Editor: Georgia Pe-Piper

Received: 28 June 2023
Revised: 22 July 2023
Accepted: 24 July 2023
Published: 26 July 2023

1. Introduction

The chemical composition of siliciclastic sedimentary rocks is an important record of the geological evolution of the continental crust through time, because some elements are quantitatively transported in the terrigenous fine fraction [1]. Of these, the rare earth elements (REEs) are the most useful because their distribution is not affected by secondary processes, and the REE patterns of fine-grained siliciclastic sediments and some elemental ratios, especially Eu/Eu*, are assumed to reflect the exposed crustal abundance in the source area [2–9]. However, weathering conditions affect the leaching of elements during the path from the protolith(s) to the sediment(s). Low-field-strength elements have a high affinity for aqueous phases, although some of them can be further partially incorporated into secondary clay minerals (see [10,11], and references therein). Mobile elements can be used to evaluate the degree of chemical weathering [12–16] and to characterize the paleoclimate and paleoprecipitation [17–23]. Consequently, the distributions of both selected major and trace elements in fine-grained siliciclastic sediments are widely used to constrain the provenance, paleoweathering, and paleoclimate conditions.

The evolution of the geology of the Mediterranean area includes peculiar phenomena, such as continental rifting during the Triassic, oceanic spreading in the Jurassic–Early Cretaceous, the closure of the Tethys from the Late Cretaceous to the Tertiary, and finally, the continental collision between the Adriatic–African plate and the European plate. This

work provides a review of the geochemistry of Meso–Cenozoic shales in the southern Apennines (Italy) to elucidate the parental affinity and paleoclimate conditions affecting shale formation to furnish a more comprehensive picture of the geological frame involved. As indicated in Table 1, all data in this paper are already published. The aim of this work was to discuss these data from different perspectives in order to give them new interpretations and to obtain new useful information.

2. Geological Framework

The southern Apennines is a fold-and-thrust belt of Adriatic origin, the formation of which mainly derived from the deformation of the African passive margin (Figure 1). The thrust belt formed during the Oligocene–Pleistocene and involved the early accretionary phases, sedimentary cover, and the ophiolitic suite of the Ligurian Ocean [24,25]. During the Miocene, the wedge consisted mainly of Meso–Cenozoic plate-forming sediments and deep-water environments and Neogene–Pleistocene foredeep deposits.

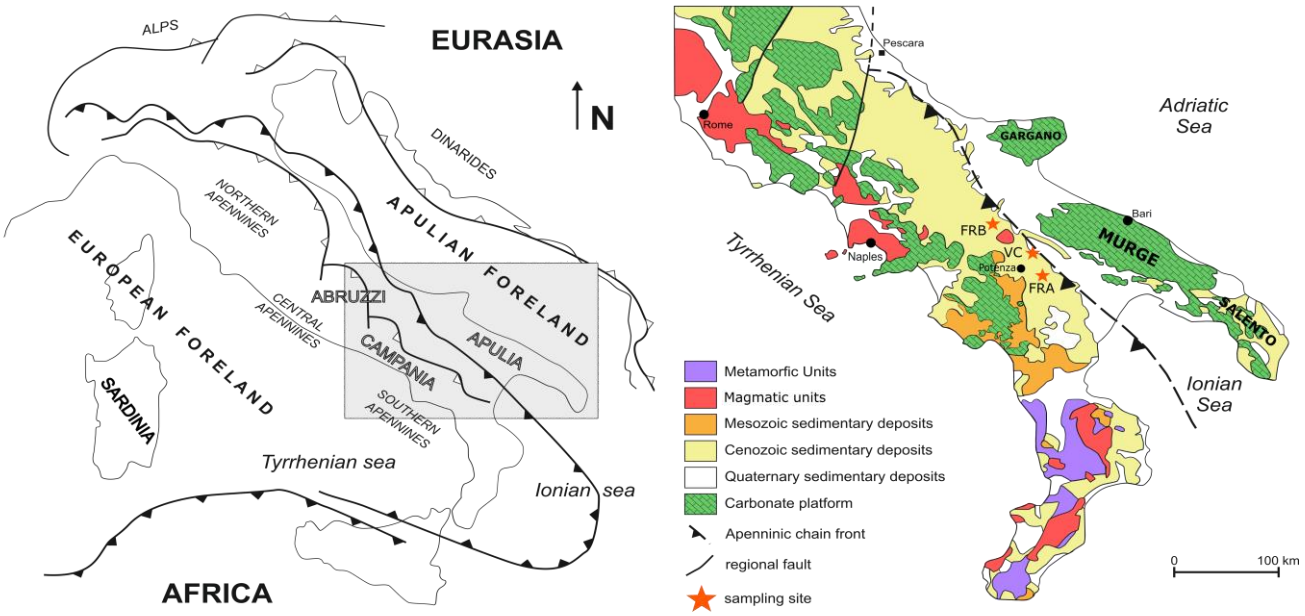

Figure 1. Geological map of southern Italy with sampling site localization.

The paleogeography of the southern Apennines in the Mesozoic is a fundamental building block for understanding the geodynamics of the western Mediterranean [26]. Considering the simplest reconstruction of the pre-Orogenic paleogeography of the southern Apennines, we observe that the African (Apulian) passive margin was characterized by a Meso–Cenozoic pelagic basin (Lagonegro basin) belonging to the Ligurian oceanic domain and lying between two carbonate platforms of the same age (Figure 2) [27–30].

The pre-Orogenic successions of Lagonegro are composed of siliciclastic, carbonate, and siliceous sediments from the Lower–Middle Triassic to the Oligo–Miocene [28]. The oldest rocks consist of shallow-water siliciclastic sediments, organogenic limestones, and, upwards, of siliciclastic deposits that indicate a progressive deepening of the basin; these rocks make up the Monte Facito Fm (Lower–Middle Triassic). Superimposed on this formation, we observe pelagic succession characterized by predominant carbonate sedimentation until the late Triassic ("Calcari con selce" Fm) that was subsequently replaced by Jurassic siliceous sedimentation ("Scisti silicei" Fm).

A significant increase in tectonic activity along the platform–basin boundaries, which resulted in uplift and erosion of the platform margins between the Late Cretaceous and the Oligocene, was responsible for the deposition of coarse-grained calcareous–clastic sediments interbedded with reddish marls and shales ("Flysch Rosso" Fm) and varicolored shales and marls ("Argille Varicolori" Fm) with the latter accumulating in a depocentral

area of the basin [28,29]. Near Campomaggiore and Vaglio di Basilicata, along the front of the southern Apennines chain, there are outcrop successions of "Flysch Rosso" Fm where shales are interbedded with siltstones and radiolarian cherts.

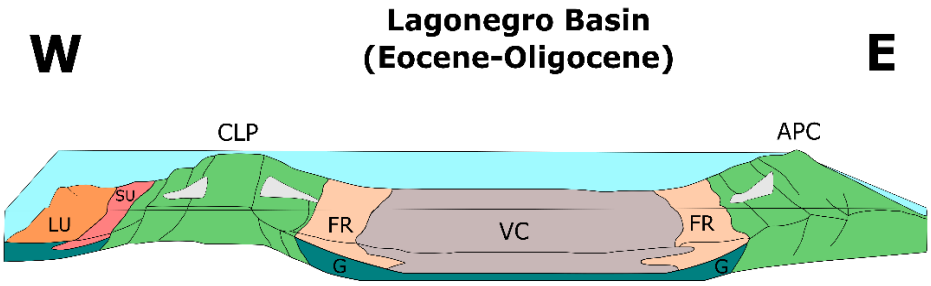

Figure 2. Paleogeographic evolution of the Lagonegro basin during the Eocene–Oligocene. Acronyms: LU and SU = Ligurian ocean and internal basinal to shelf-margin domains ('Liguride' and 'Sicilide' units); CLP and APC = Campania-Lucania and Apulian platforms; G = Flysch Galestrino (Lower–Middle Cretaceous); VC = varicoloured clays (middle Cretaceous–Oligocene), FR = Flysch Rosso (Upper Cretaceous–Oligocene). Modified from [26].

3. Sampling and Analytical Methods

For this study, a total of 52 samples were taken from four different suites, and most of them belonged to the "Flysch Rosso" Formation. Near the localities of Campomaggiore and Vaglio di Basilicata, 22 "Flysch Rosso" samples (FRA suite) were collected in a succession where shales are interbedded with siltstones and radiolarian cherts [31]. Sixteen samples of "Flysch Rosso" shales from boreholes crossing a sequence with minor calcarenite levels (FRB suite) [32] were sampled near the village of Monteverde, in the northeastern sector of the Lucanian Apennines. Finally, 14 samples (VC suite) of shales belonging to the "Argille Varicolori" Fm [3,33] were taken from a borehole crossing a pelitic sequence with rare limestones and marly limestones at the eastern boundary of the southern Apennine chain, near the village of Tolve.

Major elements were estimated by Philips (Netherland) PW 1410 X-ray fluorescence spectrometer on powdered samples using a matrix correction method [34–36]. The amount of trace elements, including REEs, was obtained by using ICP-MS at the Centre de Recherche Petrograpique et Geochimique of Vandoeuvre-les-Nancy [37]. The estimated precision and accuracy for trace element determinations were better than 5%, except for elements with a concentration of 10 ppm or lower (10%–15%). Total loss on ignition (LOI) was gravimetrically estimated after overnight heating at 950 °C. Average errors for trace elements were less than ±5%m except for elements present at 10 ppm or lower (±5–10%).

Finally, univariate, and multivariate statistics were performed with STATGRAPHICS 18 software.

4. Results and Discussion

4.1. Mineralogy and Geochemistry

The mineralogical composition of studied samples was quite homogeneous (Table 1), showing that the mineralogy was dominated by 2:1 clay minerals, such as illite and smectite, with the latter probably being derived from the weathering of illite, e.g., [38,39]. Kaolinite generally had a similar abundance to chlorite, whereas quartz and calcite were minor phases.

The results for the major and trace elements' abundances and fractionation indexes are reported in Table 2; Table 3 and as box and whiskers plots in Figures 3–5. Furthermore, The $\log(SiO_2/Al_2O_3)$ vs. $\log(Fe_2O_3/K_2O)$ classification diagram indicates that the majority of samples can be classified as shales and Fe shales (Figure 6).

Table 1. General features and the main mineralogical composition of the studied sample suites.

Locality	Lithology	Age	Formation	Sample Code	No. of Samples	Mineralogy
Campomaggiore and Vaglio di Basilicata [31]	shales interbedded with siltstones and radiolarian cherts	Late Cretaceous–Medium Miocene	Red Flysch Fm.	FRA	22	Illite > Smectite > Kaolinite, Chlorite > Quartz > Calcite
Monteverde village [32]	shales with minor calcarenite levels	Late Cretaceous–Medium Miocene	Red Flysch Fm.	FRB	16	Smectite > Illite > Kaolinite, Chlorite > Quartz > Calcite
Tolve village [3,33]	pelitic sequence with rare limestones and marly limestones	Upper Cretaceous–Lower Eocene	Argille Varicolori Fm.	VC	16	Illite > Smectite > Kaolinite, Chlorite > Quartz > Calcite

Table 2. Major oxides (wt.%) of studied shale samples.

	SiO_2	TiO_2	Al_2O_3	Fe_2O_3	MnO	MgO	CaO	Na_2O	K_2O	P_2O_5	LOI
FRA3	63.4	0.69	14.4	6.03	0.77	1.57	0.54	1.01	1.4	0.05	10.1
FRA4	58.9	0.79	16.6	8.72	0.04	1.44	0.42	0.98	1.5	0.07	10.6
FRA8	57.9	0.77	16.0	9.78	0.06	1.48	0.43	1.07	1.4	0.08	11.1
FRA10	58.5	0.80	17.8	6.51	0.25	1.47	0.57	1.01	1.4	0.10	11.7
FRA15	57.3	0.77	16.5	10.09	0.05	1.37	0.47	0.98	1.4	0.10	11.8
FRA16	67.8	0.55	12.7	6.36	0.03	1.41	0.44	0.99	1.0	0.11	8.86
FRA17	57.4	0.86	19.0	9.0	0.11	2.21	1.13	0.41	1.9	0.06	6.90
FRA18	68.5	0.69	13.7	7.99	0.04	1.47	0.36	1.02	1.5	0.08	5.41
FRA19	62.6	0.83	16.7	9.5	0.06	1.49	0.28	1.15	1.3	0.06	5.99
FRA20	59.2	0.90	18.7	9.98	0.05	1.52	0.31	1.26	1.7	0.11	5.67
FRA21	66.7	0.69	14.9	5.71	0.04	1.44	0.24	0.84	1.1	0.05	6.25
FRA22	65.8	0.70	16.6	6.48	0.07	1.68	0.37	0.59	1.1	0.06	7.03
FRA23	60.4	0.88	20.1	6.84	0.05	1.57	0.27	0.97	1.5	0.07	6.94
FRA24	68.2	0.66	14.8	7.17	0.05	1.57	0.2	0.92	1.2	0.07	6.04
FRA25	61.7	0.81	17.8	8.88	0.04	1.68	0.17	1.16	1.5	0.05	5.94
FRA26	63.1	0.73	18.2	6.6	0.05	1.86	0.31	0.71	1.3	0.05	7.14
FRA27	55.3	0.87	18.2	8.67	0.30	1.32	0.9	0.24	1.4	0.07	12.8
FRA29	67.9	0.58	13.1	5.63	0.11	1.47	0.7	0.23	1.4	0.05	8.82
FRA30	67.2	0.70	15.3	2.78	0.02	1.21	0.74	0.28	1.3	0.05	10.4
FRA31	68.9	0.65	13.6	4.12	0.09	1.24	0.72	0.25	1.3	0.05	9.10
FRA32	63.4	0.75	14.8	7.58	0.03	1.52	0.81	0.28	1.6	0.12	9.23
FRA35	58.6	0.89	17.9	5.79	0.04	2.2	0.88	0.35	2.0	0.07	11.6
FRB1	48.8	0.94	21.6	8.26	0.05	2.85	0.86	2.32	2.4	0.08	11.8
FRB2	49.1	0.89	20.6	12.53	0.05	2.8	0.38	1.35	3.1	0.09	9.05
FRB3	49.1	0.88	22	9.13	0.04	2.65	0.42	1.76	2.8	0.06	11.2
FRB4	51.9	0.92	21	9.79	0.03	3.11	0.41	1.61	3.0	0.05	8.13
FRB5	50.3	0.79	19.9	10.36	0.42	3.65	0.54	1.63	3.3	0.06	9.01
FRB6	50.7	0.85	20.5	8.97	0.05	3.36	0.5	2.27	3.2	0.06	9.68
FRB7	51.6	0.83	19.9	9.35	0.06	3.53	0.54	1.65	3.1	0.07	9.30
FRB8	49.6	0.87	20.4	9.15	0.19	3.33	0.59	1.66	2.9	0.07	11.10
FRB9	52.2	1.08	21.1	9.14	0.04	3.28	0.51	1.78	3.0	0.10	7.77
FRB10	51.6	0.95	20.8	9.26	0.04	3.16	0.63	1.72	2.8	0.09	8.97
FRB11	50.3	0.94	20.4	10.86	0.04	2.91	0.54	1.71	2.7	0.09	9.65
FRB12	50.1	0.92	20.4	8.62	0.34	3.09	1.16	2.28	2.3	0.07	11.20
FRB13	52.2	1.07	22	8.42	0.04	2.92	0.47	1.4.0	2.5	0.08	8.97
FRB14	49.7	0.97	20.2	11.73	0.03	2.69	0.74	1.85	2.4	0.09	9.65
FRB15	48.5	1.12	20.9	8.26	0.15	2.8	2.77	2.22	2.0	0.10	11.20
FRB17	50.5	1.13	21.6	9.85	0.04	2.51	0.5	1.97	2.3	0.09	9.49
VC2	49.9	1.06	24.5	7.37	0.09	1.83	2.04	1.52	2.6	0.12	8.99
VC4	46.4	1.21	28.5	6.48	0.03	1.33	0.38	3.13	1.1	0.09	11.30
VC6	50.7	0.97	22.9	9.9	0.05	2.42	0.16	1.36	4.0	0.06	7.46
VC8	50.7	1.30	25.9	6.24	0.30	1.91	0.35	1.77	2.4	0.07	9.30
VC9	49.3	1.01	24.5	9.75	0.04	1.75	0.62	1.78	2.1	0.07	9.15
VC12	52.2	1.21	23.5	7.13	0.04	2.28	0.98	1.61	3.0	0.09	7.90
VC13	49.4	1.22	23.4	9.07	0.04	2.62	1.09	1.82	3.4	0.07	7.83
VC14	50.1	1.51	27.8	4.7	0.03	1.38	0.34	1.89	2.2	0.06	10.0
VC15	51.9	1.38	27.2	5.2	0.03	1.62	0.36	1.41	2.5	0.06	8.39
VC16	53.7	1.18	24.6	6.3	0.05	1.86	0.72	1.36	2.5	0.08	7.68
VC18	53.2	1.13	27.2	4.96	0.04	1.07	0.35	0.63	1.0	0.07	10.3
VC20	50.9	1.17	26.3	6.64	0.03	1.53	0.49	0.97	1.9	0.05	10.1
VC22	49.2	1.38	28.2	6.89	0.04	1.52	0.27	1.12	1.3	0.06	10.0
VC23	49.5	1.22	23	7.29	0.04	2.55	1.04	4.0	3.5	0.10	7.71

Table 3. Trace elements (ppm) of the studied shale samples.

	Ba	Y	La	Ce	Nd	Sm	Eu	Gd	Tb	Dy	Ho	Er	Tm	Yb	Lu	LREE	HREE	ΣREE	Ce/Ce*	Eu/Eu*	$(La/Yb)_{cho}$	$(Gd/Yb)_{cho}$
FRA3	151	22	34.8	76.6	30.1	6.4	1.2	5.3	0.8	4.2	0.9	2.4	0.4	2.4	0.4	147.9	17.98	165.9	1.0	0.65	9.80	1.79
FRA4	152	24	38.5	83	33.4	6.8	1.4	6.1	1	4.4	0.9	2.4	0.4	2.5	0.4	161.7	19.52	181.2	1.0	0.68	10.41	1.98
FRA8	141	28	40.7	87	34.8	8.1	1.7	6.8	1	5	1.2	2.8	0.4	2.5	0.4	170.6	21.7	192.3	1.0	0.69	11.00	2.20
FRA10	172	28	45.7	98.8	41.2	8.8	1.8	7.6	1.2	5.6	1.1	2.9	0.4	2.5	0.4	194.5	23.52	218.0	1.0	0.67	12.35	2.46
FRA15	160	31	45	93.2	40.2	8.8	1.9	7.8	1.2	5.9	1.2	3.1	0.4	2.8	0.4	187.2	24.68	211.9	1.0	0.69	10.86	2.26
FRA16	118	31	32.2	88.2	34.1	8.7	1.9	7.8	1.2	5.4	1.1	2.7	0.4	2.4	0.4	163.2	23.22	186.4	1.2	0.70	9.07	2.63
FRA17	178	22	36	75.2	30.4	6.1	1.4	5.1	-	4.3	-	2.5	-	2.2	0.4	147.7	15.88	163.6	1.0	0.74	10.91	1.86
FRA18	190	23	32.7	66.7	29.7	6.3	1.4	5.2	-	4.3	-	2.8		2.1	0.4	135.4	16.12	151.5	1.0	0.73	10.33	1.95
FRA19	240	21	34.6	73.5	29.8	6.1	1.3	4.9	-	4.2	-	2.3		2.1	0.4	144	15.12	159.1	1.0	0.74	11.03	1.85
FRA20	185	38	42.2	85.2	37.7	8.5	1.9	7.2	-	5.9	-	3	-	2.7	0.5	173.6	21.07	194.7	0.9	0.73	10.76	2.21
FRA21	325	19	30.8	65.5	26.4	5	1.1	4	-	3.5		1.9		1.8	0.3	127.7	12.59	140.3	1.0	0.72	11.31	1.76
FRA22	204	22	33.9	74.1	28.7	5.8	1.2	4.7	-	3.9	-	2.2	-	1.9	0.3	142.5	14.26	156.8	1.0	0.69	11.81	1.98
FRA23	165	28	42.9	91.6	36.4	7.1	1.6	5.4	-	4.7	-	2.5		2.3	0.4	178	16.83	194.8	1.0	0.78	12.39	1.86
FRA24	175	15	30.3	74.6	27.9	5.8	1.3	5	-	4		2.5	-	2.1	0.4	138.6	15.22	153.8	1.1	0.72	9.75	1.91
FRA25	178	12	33.1	71.3	28.4	5.6	1.2	4.3	-	4	-	2.4	-	2.2	0.4	138.4	14.36	152.8	1.0	0.72	10.21	1.58
FRA26	126	22	31.2	70.1	25.3	5.1	1	4.2	-	3.4	-	2.1	-	1.8	0.4	131.7	12.82	144.52	1.07	0.65	11.46	1.85
FRA27	324	26	40.9	83.6	35.7	8.1	1.8	7.1	1	4.8	1	2.4	0.4	2.4	0.4	168.3	21.18	189.48	0.96	0.71	11.52	2.40
FRA29	205	19	28.4	64.3	24.9	5	1	4.6	0.7	3.2	0.7	2	0.3	1.9	0.3	122.6	14.74	137.34	1.06	0.66	10.10	1.96
FRA30	142	22	33.6	73.1	31.3	6	1.2	5.6	0.8	4.3	0.9	2.4	0.3	2.4	0.4	144	18.24	162.24	1.01	0.63	9.46	1.89
FRA31	194	21	32.7	68.3	31	6.2	1.3	5.2	0.8	3.8	0.8	2.3	0.4	2.6	0.4	138.2	17.54	155.74	0.97	0.69	8.50	1.62
FRA32	127	43	41.1	90.9	41	9.9	2.3	10	1.5	7.4	1.5	3.8	0.5	3.4	0.5	182.9	31.02	213.92	1.01	0.71	8.17	2.41
FRA35	126	28	38.9	88.6	33.5	7.4	1.6	6.4	0.8	5	1	2.6	0.4	2.6	0.4	168.4	20.84	189.24	1.07	0.71	10.11	1.99
FRB1	365	25.1	45.2	88.1	36.1	7.72	1.6	6.4	-	4.4	-	2.6	-	2.2	0.4	177.2	17.57	194.76	0.93	0.69	14.02	2.36
FRB2	341	24.1	45.7	91.2	36.1	7.63	1.6	6.3	-	4.2	-	2.6	-	2.1	0.4	180.6	17.17	197.77	0.95	0.69	14.65	2.42
FRB3	352	20.2	47.3	95.2	35.3	6.87	1.4	5.3	3.2	3.7	-	2.4	-	2	0.4	184.6	18.32	202.92	0.97	0.68	16.05	2.16
FRB4	297	19.1	45.4	91.9	37.4	7.88	1.6	6	2.6	4.2	-	2.4	-	2.1	0.4	182.6	19.27	201.83	0.96	0.70	14.54	2.31
FRB5	375	21.7	42.5	83.2	28.7	6.1	1.2	4.7	-	3.6	-	2.4	-	2.2	0.4	160.5	14.47	174.92	0.96	0.67	13.37	1.77
FRB6	514	17.1	40.6	78.4	28.3	5.7	1.2	4.8	2.8	3.5	-	2.2	-	2.1	0.4	153	16.96	169.93	0.94	0.71	13.00	1.82
FRB7	485	24.9	36.1	73.1	26.3	5.2	1.2	4.1	-	3.5	-	1.8	-	2	0.3	140.7	12.96	153.67	0.98	0.76	11.96	1.64
FRB8	374	20.6	40.8	80.3	29.1	6.03	1.3	4.9	-	3.7	-	2.2	-	2	0.4	156.2	14.4	170.62	0.96	0.72	13.58	1.95
FRB9	332	28.2	44.8	87.5	33.6	7.15	1.5	5.8	-	4.3	-	2.5	-	2.2	0.4	173.1	16.81	189.87	0.94	0.72	13.53	2.10
FRB10	308	25.6	42.7	81.8	32.6	6.64	1.4	5.6	2.9	4.1	-	2.3	-	2.2	0.4	163.7	18.86	182.52	0.92	0.71	13.29	2.07
FRB11	295	24.9	42.5	82.8	32.3	6.78	1.5	5.6	-	4.3	-	2.4	-	2.2	0.4	164.3	16.32	180.63	0.94	0.74	13.17	2.07
FRB12	442	24.1	40.4	78.7	30.8	6.45	1.4	5.3	-	4	-	2.3	-	2	0.4	156.4	15.4	171.77	0.94	0.72	13.65	2.16

Table 3. *Cont.*

	Ba	Y	La	Ce	Nd	Sm	Eu	Gd	Tb	Dy	Ho	Er	Tm	Yb	Lu	LREE	HREE	ΣREE	Ce/Ce*	Eu/Eu*	$(La/Yb)_{cho}$	$(Gd/Yb)_{cho}$
FRB13	296	26.5	41.6	76.3	28.7	5.53	1.2	3.8	-	3.6	-	1.8	-	2	0.3	152.2	12.75	164.93	0.90	0.80	13.77	1.52
FRB14	212	23.8	43.1	83.2	33.7	6.82	1.5	5.7	2.5	4.2	-	2.4	-	2.1	0.4	166.8	18.7	185.51	0.93	0.75	13.79	2.17
FRB15	245	27.8	46.9	87.3	35.1	7.38	1.6	6.1	-	4.7	-	2.6	-	2.4	0.4	176.7	17.74	194.41	0.90	0.74	13.32	2.06
FRB17	235	31	47.9	92.9	38.9	7.79	1.8	6.2	-	5	-	2.5	-	2.4	0.4	187.4	18.24	205.65	0.92	0.78	13.25	2.07
VC2	148	35	51.3	99.6	40.5	8.29	1.7	6.8	0.8	5.1	-	3	-	2.5	0.4	199.7	20.31	220.03	0.93	0.69	13.99	2.21
VC4	108	34	55.5	113	45.5	8.85	1.8	6.8	0.9	5.6	-	3.1	-	3	0.5	222.7	21.67	244.32	0.97	0.69	12.37	1.81
VC6	198	22	54.1	107	42.7	7.33	1.4	5.6	0.8	4.2	-	2.6	-	2.7	0.5	210.6	17.71	228.35	0.94	0.64	13.40	1.66
VC8	198	29	62.8	118	47.6	9.23	1.7	6.4	0.7	5	-	2.9	-	2.8	0.5	237.3	19.97	257.3	0.90	0.66	15.31	1.87
VC9	167	20	47.6	85.6	31.1	5.96	1.3	5	1.2	4.1	-	2.3	-	2.2	0.4	170.2	16.52	186.74	0.89	0.74	14.34	1.79
VC12	235	33	57.6	103	46	9.28	1.8	7.3	0.9	5.7	-	3.2	-	2.9	0.5	216	22.33	238.37	0.85	0.68	13.62	2.08
VC13	758	33	74.7	138	57.9	10.6	1.9	7.5	0.9	5.8	-	3.3	-	3.4	0.6	281.6	23.27	304.88	0.89	0.64	15.03	1.81
VC14	145	31	80.9	136	62.4	11	1.8	6.8	0.7	5.8	-	3.4	-	3.3	0.6	290.4	22.41	312.82	0.81	0.65	16.57	1.67
VC15	237	28	75.7	130	59.3	10.4	1.7	6.3	0.7	5.3	-	3.3	-	3.2	0.5	274.9	21	295.87	0.82	0.65	16.23	1.63
VC16	151	30	60.1	97.7	45.1	8.36	1.6	6.3	0.9	5.1	-	3.1	-	2.8	0.5	211.3	20.36	231.65	0.78	0.67	14.40	1.82
VC18	130	28	44.8	78.7	37.2	7.05	1.4	5.4	0.7	4.6	-	2.6	-	2.6	0.5	167.8	17.8	185.58	0.83	0.70	11.56	1.66
VC20	220	24	56.4	106	42.9	8.05	1.5	5.4	1	4.7	-	2.9	-	2.6	0.5	213	18.53	231.57	0.90	0.68	14.90	1.72
VC22	143	31	52	99.1	41.2	7.13	1.4	4.9	0.4	4.7	-	2.8	-	2.9	0.5	199.3	17.49	216.78	0.91	0.70	12.23	1.38
VC23	171	22	66.7	117	54	10.3	1.9	7.6	0.8	6.2	-	3.7	-	3.4	0.6	248.3	24.15	272.49	0.84	0.66	13.25	1.80

Note: $Eu/Eu^* = [Eun/\sqrt{(Smn \cdot Gdn)}]$; $Ce/Ce^* = [Cen/\sqrt{(Lan \cdot Prn)}]$.

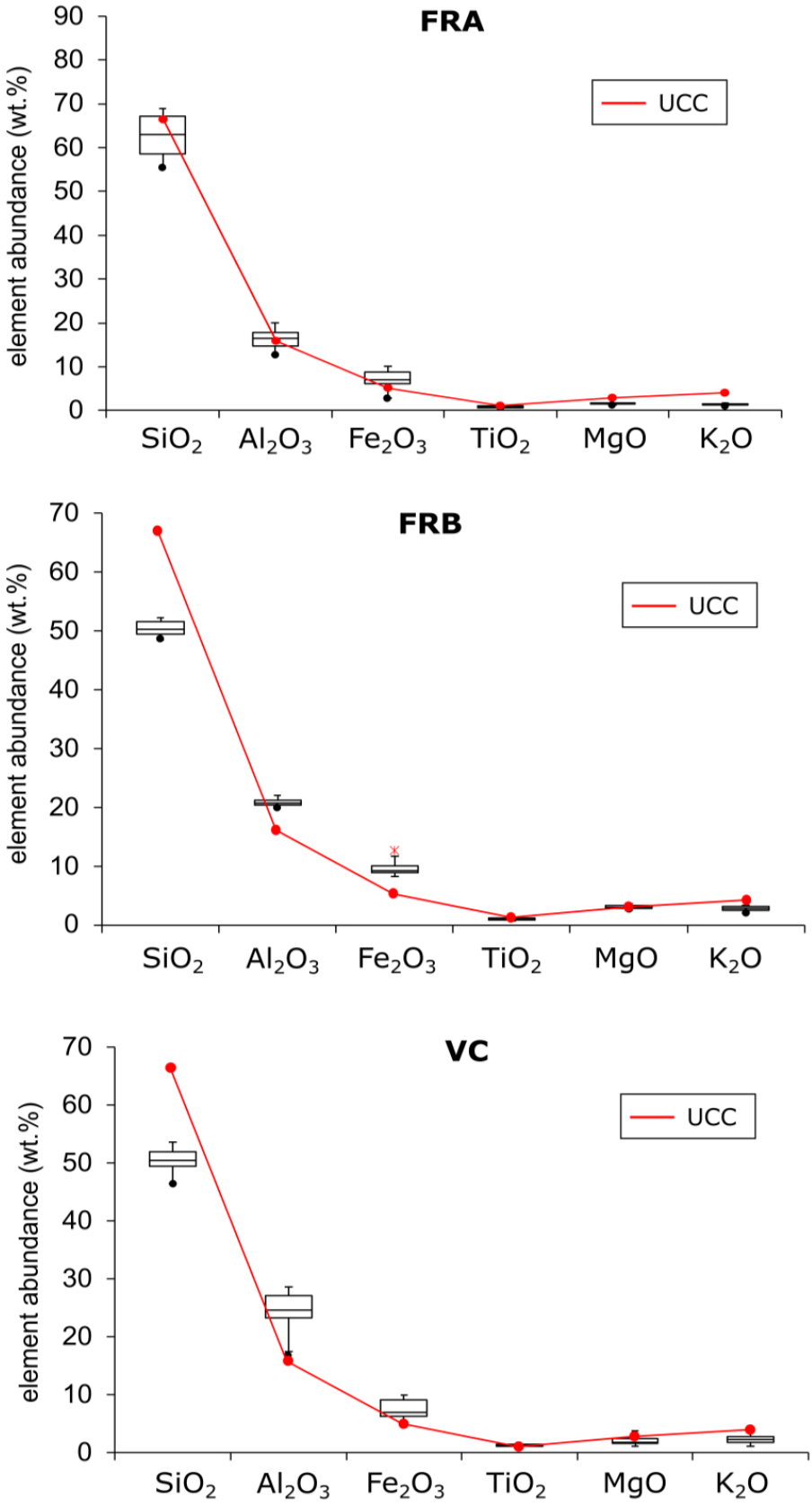

Figure 3. Box plot for the major oxide abundance (wt.%) in the studied samples. UCC values are taken from [1].

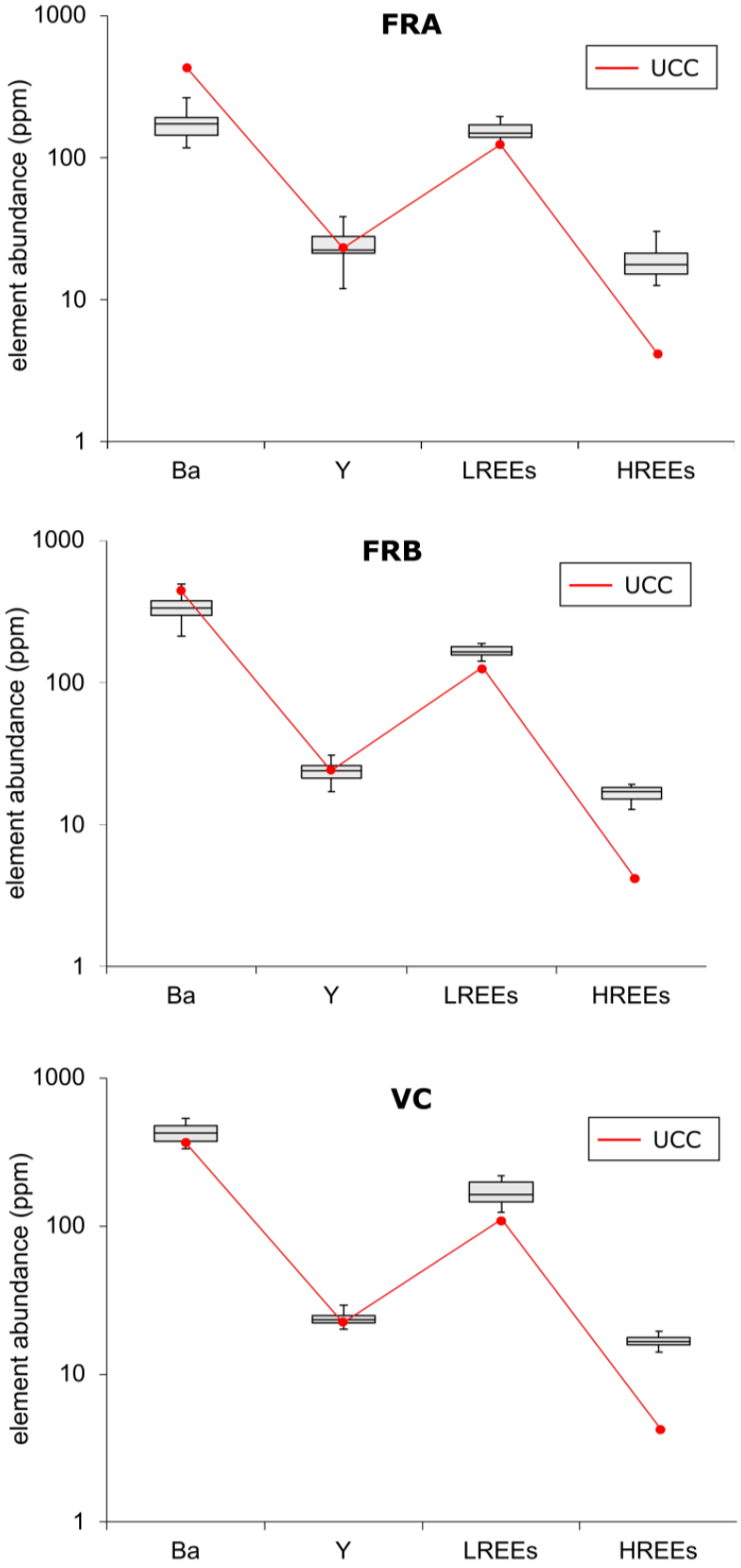

Figure 4. Box plot of the trace element abundance (ppm) in the studied samples. UCC values are taken from [1].

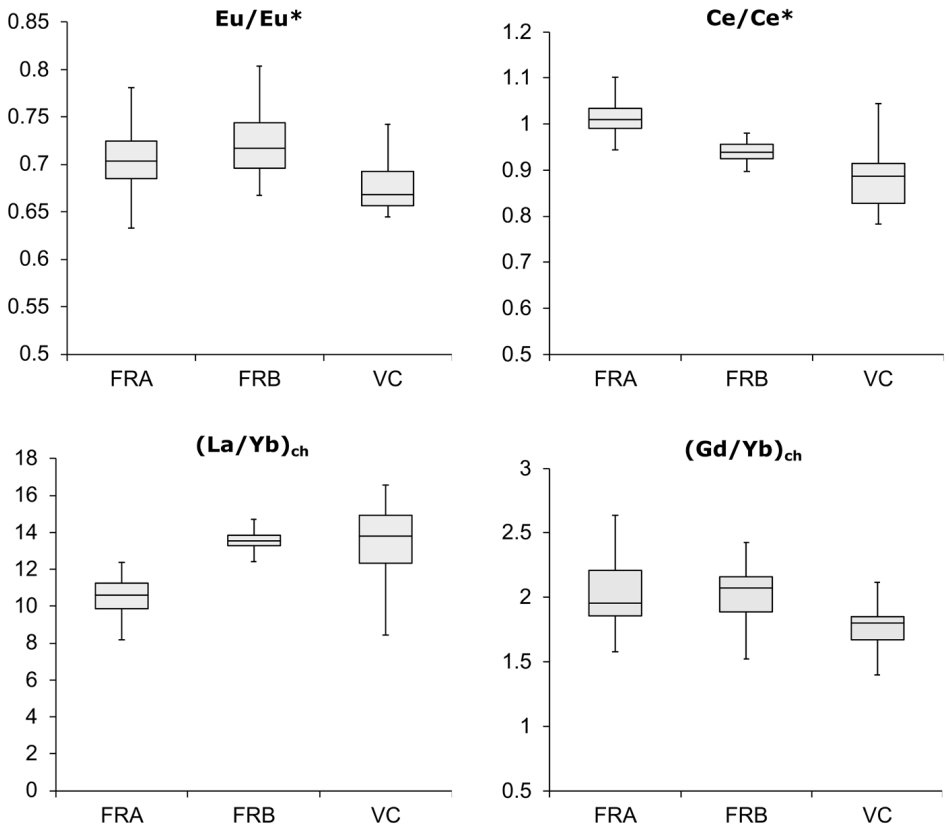

Figure 5. Box plot for Ce and Eu anomalies and La/Yb and Gd/Yb fractionation indices of the studied samples.

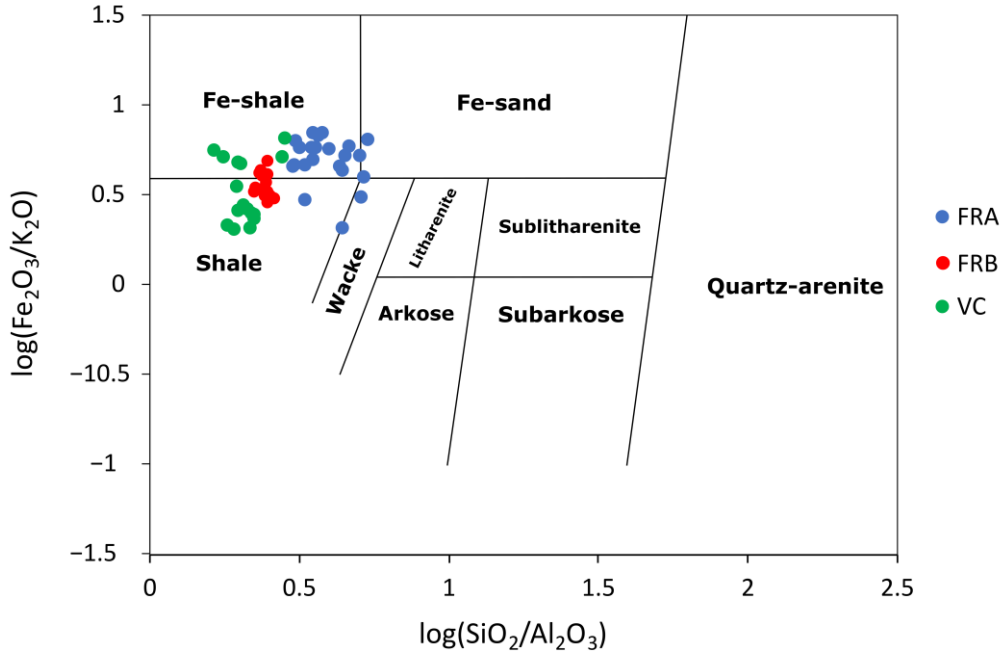

Figure 6. Herron's classification diagram [39] using $\log(SiO_2/Al_2O_3)$-$\log(Fe_2O_3/K_2O)$.

Chemical analyses show that the most abundant major oxides are SiO_2, (median suite FRA = 63.1 ± 4.39 wt.%; median suite FRB; 50.32 ± 1.22 wt.%; median suite VC = 50.38 ± 1.79 wt.%), Al_2O_3 (median suite FRA = 16. 52 ± 2.07 wt.%; median suite FRB = 20.71 ± 0.69 wt.%; median suite VC = 25.3 ± 1.94 wt.%), and Fe_2O_3 (median suite FRA = 7.17 ± 1.93 wt.%; median suite FRB = 9.2 ± 1.23 wt.%; median suite VC = 6.77 ± 1.57 wt.%) (Figure 4). The

shales show lower SiO_2 and K_2O contents and higher Al_2O_3 and Fe_2O_3 contents with respect to the Upper Continental Crust (hereafter, the UCC, [1] and, consistently, are classified as Fe shales and shales with very few samples of the FRA subset, which result in wacke and Fe sand [40].

Regarding the trace elements, Ba shows median values of 173.5 ± 55.49 (FRA suite), 336.45 ± 84.97 ppm (FRB suite), and 169.0 ± 155.8 ppm (VC suite). The high value of the Ba standard deviation in the VC suite is related to a single sample (VC13) that shows Ba abundance of 758 ppm and more CaO enrichment with respect to other samples. Y displays median values of 22.5 ± 6.98 ppm, 24.5 ± 3.61 ppm, and 29.5 ± 4.68 ppm, respectively, for the FRA, FRB, and VC suites.

The ΣREE median value is 189.4 ± 40.5, and the chondrite normalized REE patterns (Figure 7) are characterized by a typical shale-like trend with enrichment of LREEs ($(La/Yb)_{ch}$ median = 12.70 ± 2.03), a flat distribution of HREEs ($(Gd/Yb)_{ch}$ median = 1.93 ± 0.27), the absence of Ce anomalies (Ce/Ce* median = 0.95 ± 0.08), and negative Eu anomalies (Eu/Eu* median = 0.70 ± 0.04). It must be noted that the lack of a positive Ce anomaly excludes prevailing intense and long-lasting weathering during subaerial oxidizing environmental conditions [38]. Further details can be found in [3,9,39–42].

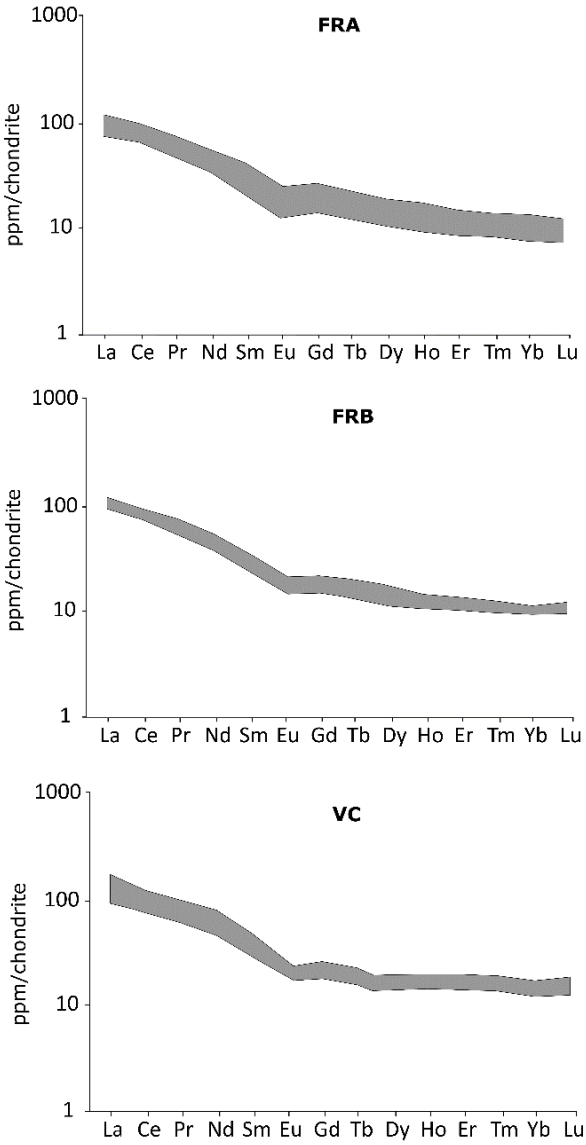

Figure 7. Chondrite-normalized distribution patterns of REEs in the studied samples.

4.2. Factors Affecting the Distribution of Elements

An R-mode factor analysis, classical type of factoring, was performed to evaluate interelemental relationships among the major oxides, Ba, Y, LREE, and HREE. Factors were extracted with the STATGRAPHICS 18 package. This operation was performed using a standardized correlation matrix and thereby weighting all the variables equally during factor calculations. The communalities provide an index of the efficiency of the proposed set of factors [43], and the magnitude of the communalities calculated in this study suggests that most of the original variance is still accounted for by the present set of factors. Three factors explain 91.7% of the total variance in the geochemical database (Table 4).

Table 4. Factor Loading Matrix After Varimax Rotation.

	Factor	**Factor**	**Factor**
	1	2	3
SiO_2	−0.72		
TiO_2	0.96		
Al_2O_3	0.93		
Fe_2O_3			
MgO		0.98	
CaO			
Na_2O			
K_2O		0.77	
P_2O_5			0.93
Ba			
Y			0.77
LREE	0.82		
HREE			0.72
Var.%	47.7	28.2	15.8

Note: The numbers are the weights of the variables in the extracted factors. Variables with weights of less than 0.70 were omitted.

The first factor (F1; Var.% = 47.7) includes significant positive weightings for Al_2O_3, TiO_2, and LREE and a negative weighting for SiO_2. Titanium, Al, and LREE are low-solubility elements characterized by low to very low residence times in oceanic water and seawater to the upper crust partition coefficient [1]. The potential of these elements to be fractionated during the sedimentary process, especially in the source rock(s)–shale transformation, is thus negligible. Further, the LREE covariance with Al_2O_3 and TiO_2 supports the idea that these elements in shales are controlled by clay minerals or occur as detrital tiny crystals in the clayey grain-size fraction [33,40]. Silica in our shales is mainly hosted in 2:1 and 1:1 clay minerals, and its negative weighting can be related to illite → smectite → kaolinite evolution during a more intense weathering stage, also promoting the residual accumulation of elements characterized by lower solubility, such as Ti, Al, and LREE.

The second factor (F2; Var.% = 28.2) has significant and positive weightings for MgO and K_2O. In 2:1 clay minerals, which in these shales are the most abundant phases, K^+ and Mg^{2+} occur in the interlayer spaces of illite and smectite, respectively. Further, Mg^{2+} may also substitute Al^{3+} in the octahedral sheets. Both of these cations can be released to the soil solutions during the illite → smectite → kaolinite weathering, thus explaining the K_2O-MgO covariance associated with F2.

The third factor (F3; Var.% = 15.8) shows significant and positive weightings for P_2O_5, Y, and HREE. The yttrium geochemical affinity for the HREE is well known, and both may be distributed by phosphate minerals in a variety of sedimentary rocks [44,45] and shales [3,46]. F3, coupled with F1, indicates fractionation between LREE and HREE+Y in

the southern Apennines shales, suggesting that an index such as $(La/Yb)_{ch}$ non-necessarily records the source area.

4.3. Paleoweathering

It is well known that alkali and alkaline–earth elements are mobile elements, and their depletion in siliciclastic and residual sediments is generally related to chemical weathering processes, producing a depletion of mobile elements (i.e., Ca, Na, and K) and an enrichment of immobile elements such as Al, and the relationship between mobile and immobile elements was used to reconstruct the weathering conditions affecting the source area. The chemical index of alteration (hereafter, CIA) [12] is the most commonly used index to define broad palaeoweathering conditions in siliciclastic and residual sediments e.g., [3,16,47,48]. The CIA was calculated using the formula (molecular proportions): CIA = $[Al_2O_3/(Al_2O_3 + CaO^* + Na_2O + K_2O)] \times 100$, where CaO* is the amount of CaO only regarding silicate minerals. The CIA value for non-weathered upper crustal rocks is approximately 50%, whereas highly weathered residual rocks have CIA values of higher than 90%.

In the analyzed samples, the median CIA values of the three subsets were in the 80–85% range (FRA: CIA = 85 ± 2; FRB: CIA = 80 ± 2; VC: CIA = 85 ± 5), suggesting that southern Apennines shales largely formed through prevailing moderate to intense weathering. Further, the reasonably homogeneous CIA values in the southern Apennines shales appear to rule out non-steady-state weathering conditions, usually related to active tectonism. The A-CN-K diagram (Figure 8) illustrates a composite trend starting from a UCC-like protolith, initially pointing toward an illite composition (FRB subset), and further moving toward the A apex and kaolinite formation (FRA and VC subsets).

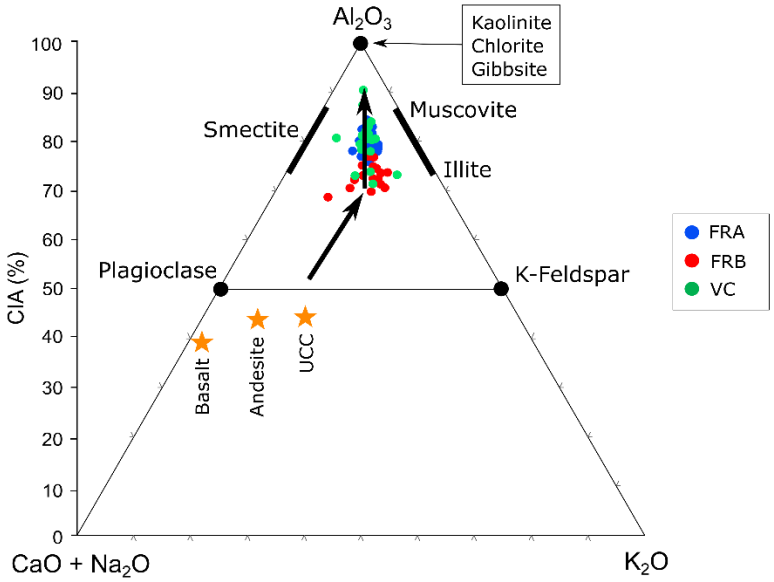

Figure 8. A (Al_2O_3) − CN ($CaO^* + Na_2O$) − K (K_2O) ternary diagram (molecular proportions; Nesbitt and Young, 1982). The UCC, andesite, and basalt values are taken from [1].

The chemical composition of paleosoils can also be used to assess paleoprecipitation (see [49], and references therein), through the climofunctions CIA-K (100 × (Al/(Al + Ca + Na)) [50] and the related mean annual precipitation (MAP(mm/y) = $221.1e^{0.0197(CIA\text{-}K)}$ [16] and CALMAG (100 × (Al/(Al + Ca + Mg)) [20,21], MAP(mm/y) = 22.69(CALMAG)–435.8 (Table 5)). The picture depicted by the CIA-K and CALMAG is consistent with the CIA and A-CN-K diagram involving higher median values for the FRA (CIA-K = 90 ± 2; MAP = 1309 ± 44 mm/y; CALMAG = 87 ± 2; MAP = 1548 ± 51 mm/y) and VC (CIA-K = 90 ± 45; MAP = 1286 ± 111 mm/y; CALMAG = 90 ± 4; MAP = 1610 ± 83 mm/y) subsets than the FRB subset (CIA-K = 87 ± 3. MAP = 1214 ± 76 mm/y; CALMAG = 82 ± 3; MAP = 1444 ± 59 mm/y), suggesting that the latter was affected by drier climatic conditions (Figure 9).

Table 5. CIA, CIA-K, and CALMAG values.

Samples	CIA (%)	CIA-K (%)	MAP-CIA-K (mm/year)	CALMAG (%)	MAP-CALMAG (mm/year)
FRA3	83	87	1221.76	85	1495.36
FRA4	85	90	1282.73	88	1566.31
FRA8	84	88	1256.46	88	1550.73
FRA10	86	89	1271.69	88	1559.37
FRA15	85	89	1273.24	88	1566.33
FRA16	84	86	1208.15	85	1497.06
FRA17	85	90	1295.90	82	1434.69
FRA18	83	88	1238.97	86	1524.32
FRA19	86	89	1277.94	89	1581.58
FRA20	85	90	1283.48	90	1599.20
FRA21	87	91	1316.40	88	1568.44
FRA22	89	93	1363.13	87	1545.49
FRA23	88	92	1349.32	90	1613.35
FRA24	86	90	1307.39	88	1556.48
FRA25	86	91	1309.60	89	1589.45
FRA26	89	93	1367.47	88	1554.74
FRA27	88	92	1350.03	87	1537.42
FRA29	85	91	1325.64	83	1455.59
FRA30	87	92	1338.12	87	1528.21
FRA31	85	91	1323.49	85	1493.66
FRA32	84	91	1317.59	84	1469.72
FRA35	85	91	1331.75	83	1445.00
median	85	91	1308.50	87	1548.11
st.dev.	1.68	1.74	43.99	2.23	50.63
FRB1	79	83	1129.91	83	1448.89
FRB2	81	90	1283.93	85	1487.88
FRB3	82	88	1242.23	86	1515.03
FRB4	81	88	1249.98	84	1462.64
FRB5	78	87	1216.99	80	1385.25
FRB6	78	84	1154.25	82	1423.71
FRB7	79	87	1214.73	81	1395.72
FRB8	80	87	1214.68	82	1416.73
FRB9	80	87	1218.04	83	1439.33
FRB10	80	86	1207.55	82	1432.92
FRB11	81	87	1213.38	83	1456.84
FRB12	78	81	1086.14	80	1379.44
FRB13	84	89	1281.11	85	1487.09
FRB14	80	85	1170.90	83	1452.22
FRB15	75	75	970.04	75	1267.54
FRB17	82	86	1203.67	86	1513.96
median	80	87	1214.03	83	1444.11
st.dev.	1.93	3.43	75.88	2.60	58.94
VC2	80	83	1136.43	83	1458.25
VC4	86	85	1181.96	93	1682.57
VC6	81	92	1334.40	89	1572.55
VC8	85	90	1289.39	91	1622.88
VC9	85	88	1245.81	90	1598.06
VC12	81	87	1215.74	86	1508.73
VC13	79	85	1181.38	84	1469.89
VC14	86	90	1293.68	93	1678.67
VC15	86	92	1338.78	92	1653.84
VC16	84	90	1282.85	89	1579.69
VC18	93	95	1435.72	94	1700.33
VC20	89	93	1369.53	92	1642.69
VC22	91	94	1389.33	93	1676.12
VC23	73	77	996.64	84	1475.38
median	85	90	1286.12	90	1610.47
st.dev.	5.10	4.67	111.23	3.65	82.78

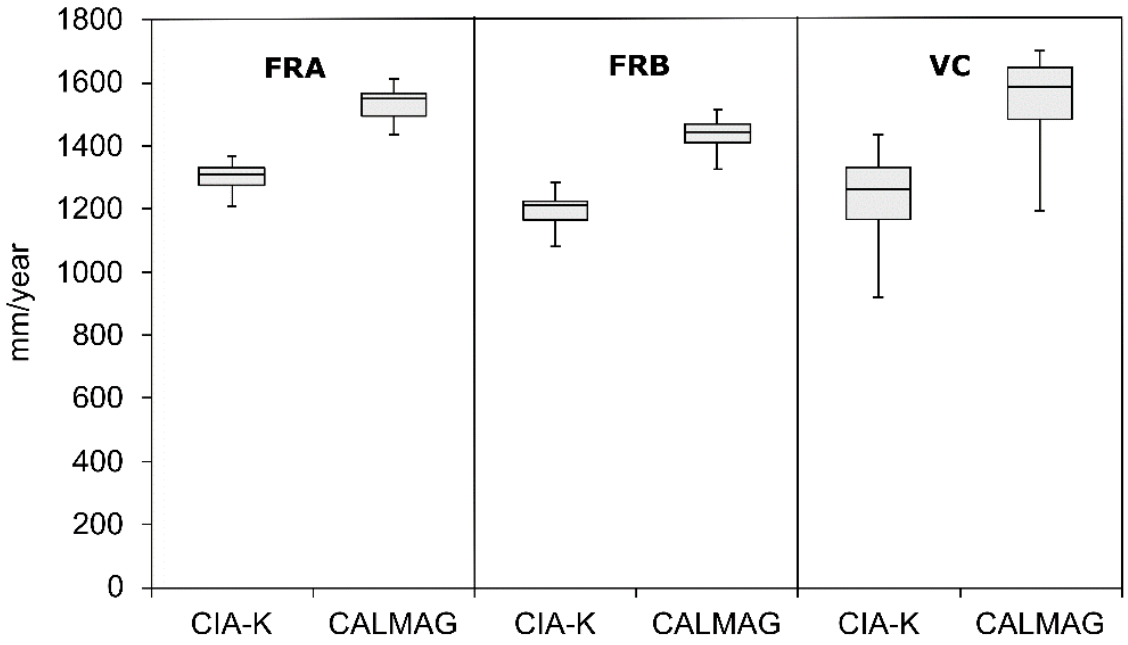

Figure 9. Box plot showing the values of CIA-K and CALMAG (mm/y) in the studied shales.

4.4. Provenance

Proxies based on low-mobility elements, affected by minor fractionation during intense weathering and recording chemical differentiation, are used to identify the parent rock(s) of shales [2,3,7,8,10,11,14,15]. Among them, the Eu anomaly is retained as the more conservative provenance proxy [3,10,11,14].

In the southern Apennine shales, the value of the Eu/Eu* is close to the UCC value (Eu/Eu* = 0.65), indicating crustal provenance and ruling out a significant mafic supply. The Sm/Nd ratio shows similar values to Eu/Eu*, reflecting that chemical differentiation and only minor fractionation of Sm and Nd occurs during weathering [51]. Further, the observed covariance between Al_2O_3 and TiO_2 in these shales excludes any fractionation between Ti and Al, suggesting the effectiveness of the Ti/Al ratio as the provenance proxy. In the Eu/Eu* vs. Sm/Nd (Figure 10) and Eu/Eu* vs. Ti/Al diagrams (Figure 11) the shales fall far from the average value for basalt and quite close to the UCC values, thus excluding any mafic provenance. It is worth nothing that the Eu/Eu* median is, with respect to the UCC, slightly higher (0.70 ± 0.04), with a shift toward the value of the Archean shales (Eu/Eu* = 0.73; [52]), suggesting the presence of a less differentiated component. Several shales show $(Gd/Yb)_{ch} > 2$, which is usually associated with Archean terranes (Figure 12), e.g., [52,53]. Thus, the values of the $(Gd/Yb)_{ch}$ ratio suggest that southern Apennine shales likely incorporated material derived from exposed African Archean terranes or, more likely, ancient sediments derived from African Archean terranes through a cannibalistic process [9] (Figure 12). These findings suggest that the Lagonegro basin was connected through a southern entry area with a continental margin, the African cratonic area, providing siliciclastic detritus according to what was proposed for other siliciclastic sediments of the Lagonegro basin (Figure 13) [41].

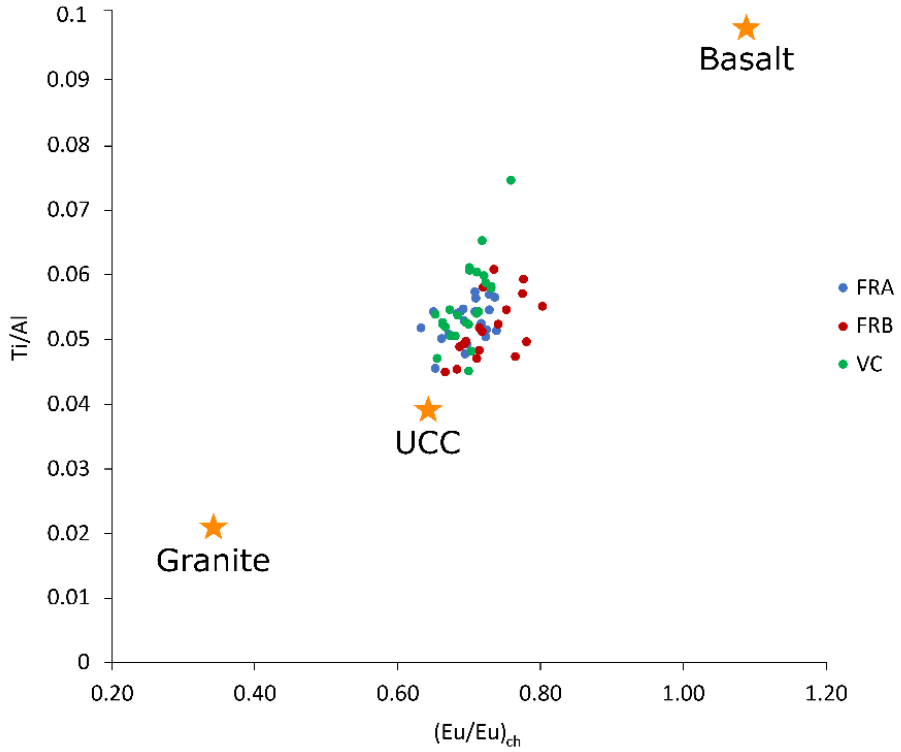

Figure 10. Eu/Eu* vs. Ti/Al binary diagram. The UCC and basalt values were taken from [1]; granite values were taken from [52].

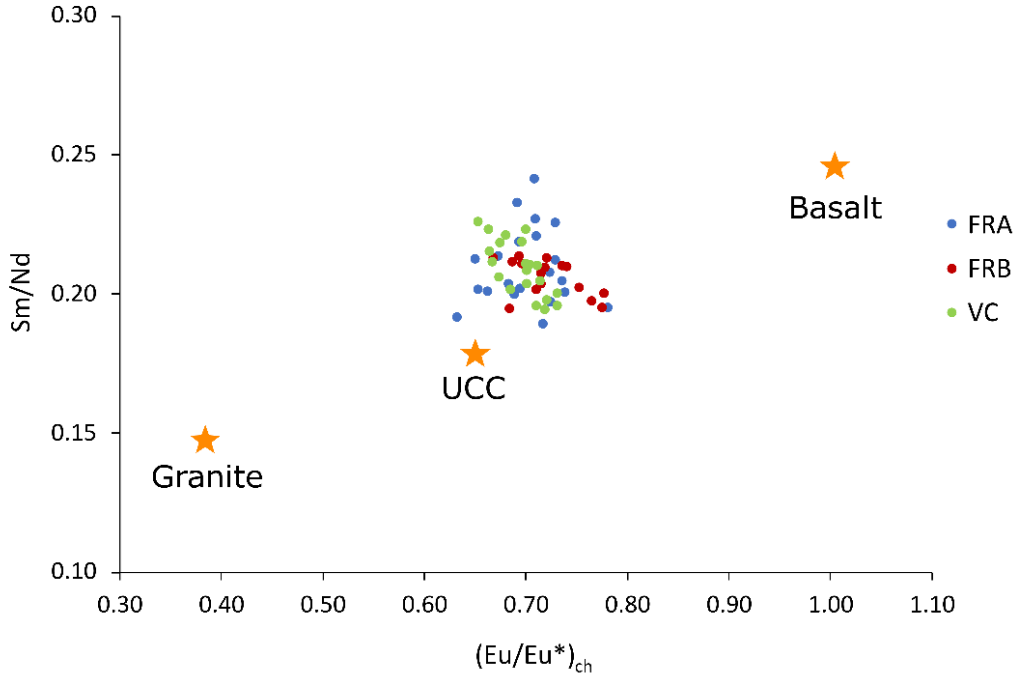

Figure 11. Eu/Eu* vs. Sm/Nd binary diagram. The UCC and basalt values were taken from [1]; granite values were taken from [52].

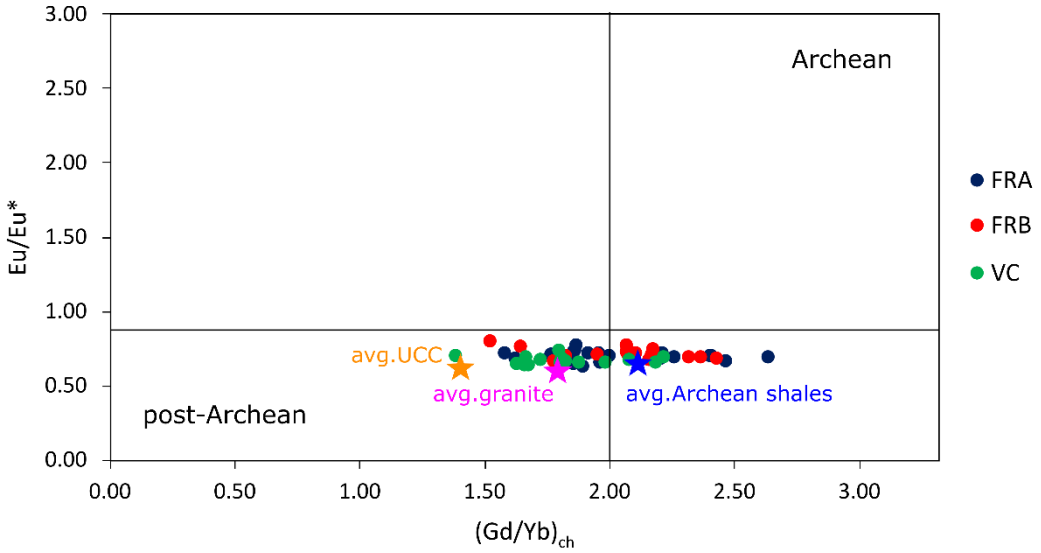

Figure 12. $(Gd/Yb)_{ch}$ vs. Eu/Eu* classification diagram. The fields follow [53]. The UCC values were taken from [1]; granite and shale values were taken from [52].

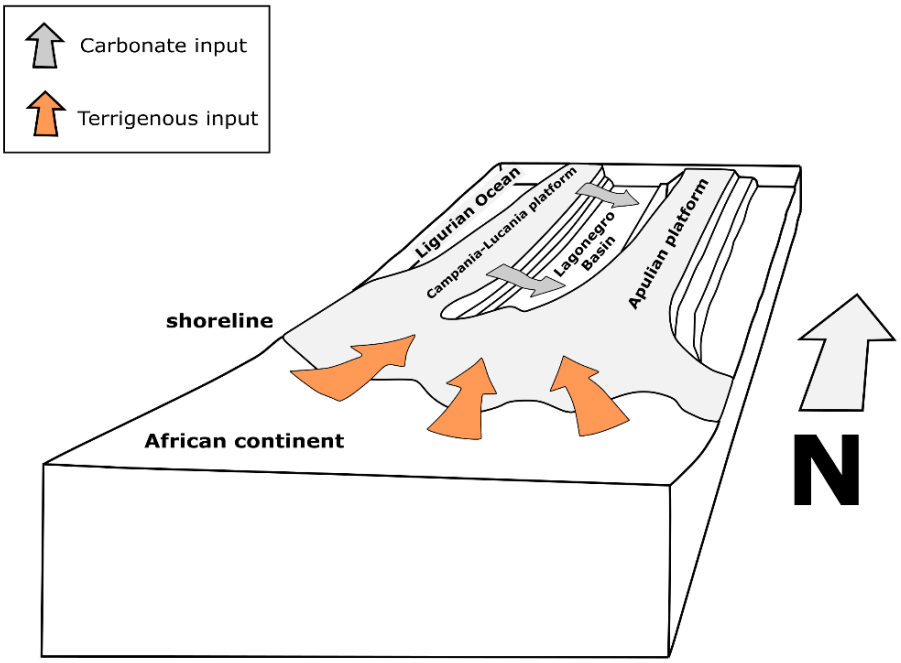

Figure 13. Schematic Eocene–Oligocene palaeogeography of the Apulian margin including the Lagonegro basin, showing the connection to the African cratonic area through a southern entry area. Modified from [41].

5. Conclusions

The different suites of southern Apennine shales largely share similar mineralogical and geochemical features. The samples are dominated by 2:1 clay minerals and are Fe shales and shales showing, with respect to the UCC, lower SiO_2 and K_2O and higher Al_2O_3 and Fe_2O_3 contents. The different factors extracted by R-mode factor analysis indicate Ti, Al, and LREE (F1) and K_2O-MgO (F2) covariance, likely related to the illite → smectite → kaolinite evolution during weathering. HREE and Y are distributed by phosphate minerals, suggesting LREE/HREE fractionation. The CIA paleoweathering proxy rules out non-steady-state weathering conditions and indicates that the source area was affected by moderate to intense weathering, which is also consistent with what is depicted by the CIA-K and CALMAG paleoweathering proxies. The paleoprecipitation values derived

from the CIA-K and CALMAG indices show median values in the 1214–1610 mm/y range with the FRB subset affected by drier climatic conditions.

The Eu/Eu*, Sm/Nd, and Ti/Al provenance ratios point toward an UCC-like source excluding any mafic supply and suggesting that the Lagonegro Basin was connected, through a southern entry area, with the African cratonic area. However, the Eu/Eu* median value of the southern Apennine shales is almost similar to the value of the Archean shales, possibly indicating a less differentiated component. In addition, in many samples, the $(Gd/Yb)_{ch}$ ratio is >2, indicating that the shales likely incorporated ancient sediments derived from African Archean terranes through a cannibalistic process.

Author Contributions: Conceptualization, R.B., G.R. and G.M.; sampling activity G.M.; laboratory analysis and methodology, G.M.; writing—original draft preparation, R.B., G.R. and G.M.; supervision, G.M. All authors have read and agreed to the published version of the manuscript.

Funding: This research received no external funding.

Data Availability Statement: Not applicable.

Conflicts of Interest: The authors declare no conflict of interest.

References

1. Taylor, S.R.; McLennan, S.M. *The Continental Crust: Its Composition and Evolution*; Blackwell: Oxford, UK, 1985.
2. McLennan, S.M.; Hemming, S.; McDaniel, D.K.; Hanson, G.N. Geochemical approaches to sedimentation, provenance, and tectonics. *Geol. Soc. Am. Spec. Pap.* **1993**, *284*, 21–40.
3. Mongelli, G.; Critelli, S.; Perri, F.; Sonnino, M.; Perrone, V. Sedimentary recycling, provenance and paleoweathering from chemistry and mineralogy of Mesozoic continental red bed mudrocks, Peloritani Mountains, Southern Italy. *Geochem. J.* **2006**, *40*, 197–209. [CrossRef]
4. Fedo, C.M.; Eriksson, K.A.; Krogstad, E.J. Geochemistry of shales from the Archean (~3.0 Ga) Buhwa Greenstone Belt, Zimbabwe: Implications for provenance and source-area weathering. *Geochim. Cosmochim. Acta* **1996**, *60*, 1751–1763. [CrossRef]
5. Hassan, S.; Ishiga, H.; Roser, B.P.; Do Zen, K.; Naka, T. Geochemistry of Permian–Triassic shales in the Salt Range, Pakistan: Implications for provenance and tectonism at the Gondwana margin. *Chem. Geol.* **1999**, *158*, 293–314. [CrossRef]
6. Bauluz, B.; Mayayo, M.J.; Fernandez-Nieto, C.; Gonzales Lopez, J.M. Geochemistry of Precambrian and Paleozoic siliciclastic rocks from the Iberian Range (NE Spain): Implications for source-area weathering, sorting, provenance, and tectonic setting. *Chem. Geol.* **2000**, *168*, 135–150. [CrossRef]
7. Cullers, R.L.; Podkovyrov, V.N. Geochemistry of the Mesoproterozoic Lakhanda shales in southeastern Yakutia, Russia: Implications for mineralogical and provenance control, and recycling. *Precambrian Res.* **2000**, *104*, 77–93. [CrossRef]
8. Condie, K.C.; Lee, D.; Farmer, G.L. Tectonic setting and provenance of the Neoproterozoic Uinta Mountain and Big Cottonwood groups, northern Utah: Constraints from geochemistry, Nd isotopes, and detrital modes. *Sediment. Geol.* **2001**, *141*, 443–464. [CrossRef]
9. Mongelli, G. Rare earth elements in Oligo-Miocenic pelitic sediments from Lagonegro basin, Southern Apennines, Italy: Implication for provenance and source area weathering. *Int. J. Earth Sci.* **2004**, *93*, 612–620. [CrossRef]
10. Sinisi, R.; Mongelli, G.; Mameli, P.; Oggiano, G. Did the Variscan relief influence the Permian climate of Mesoeurope? Insights from geochemical and mineralogical proxies from Sardinia (Italy). *Palaeogeogr. Palaeoclimatol. Palaeoecol.* **2014**, *396*, 132–154. [CrossRef]
11. Mameli, P.; Mongelli, G.; Sinisi, R.; Oggiano, G. Weathering products of a dismantled Variscan basement. Minero-chemical proxies to insight on Cretaceous palaeogeography and Late Neogene palaeoclimate of Sardinia (Italy). *Front. Earth Sci.* **2020**, *8*, 290. [CrossRef]
12. Nesbitt, H.W.; Young, G.M. Early Proterozoic climates and plate motions inferred from major element chemistry of lutites. *Nature* **1982**, *299*, 715–717. [CrossRef]
13. Harnois, L. The CIW index: A new chemical index of weathering. *Sediment. Geol.* **1988**, *55*, 319–322. [CrossRef]
14. Fedo, C.M.; Eriksson, K.A.; Blenkinsop, T.G. Geologic history of the Archean Buhwa Greenstone Belt and surrounding granite–gneiss terrane, Zimbabwe, with implications for the evolution of the Limpopo Belt. *Can. J. Earth Sci.* **1995**, *32*, 1977–1990. [CrossRef]
15. Perri, F. Reconstructing chemical weathering during the Lower Mesozoic in the Western-Central Mediterranean area: A review of geochemical proxies. *Geol. Mag.* **2018**, *155*, 944–954. [CrossRef]
16. Perri, F. Chemical weathering of crystalline rocks in contrasting climatic conditions using geochemical proxies: An overview. *Palaeogeogr. Palaeoclimatol. Palaeoecol.* **2020**, *556*, 109873. [CrossRef]
17. Sheldon, N.D.; Retallack, G.J.; Tanaka, S. Geochemical climofunctions from North American soils and application to paleosols across the Eocene-Oligocene boundary in Oregon. *J. Geol.* **2002**, *110*, 687–696. [CrossRef]

18. Rasmussen, C.; Tabor, N.J. Applying a quantitative pedogenic energy model across a range of environmental gradients. *Soil Sci. Soc. Am. J.* **2007**, *71*, 1719–1729. [CrossRef]
19. Lukens, W.E.; Nordt, L.C.; Stinchcomb, G.E.; Driese, S.G.; Tubbs, J.D. Reconstructing pH of paleosols using geochemical proxies. *J. Geol.* **2018**, *126*, 427–449. [CrossRef]
20. Lukens, W.E.; Stinchcomb, G.E.; Nordt, L.C.; Kahle, D.J.; Driese, S.G.; Tubbs, J.D. Recursive partitioning improves paleosol proxies for rainfall. *Am. J. Sci.* **2019**, *319*, 819–845. [CrossRef]
21. Nordt, L.C.; Driese, S.D. New weathering index improves paleorainfall estimates from Vertisols. *Geology* **2010**, *38*, 407–410. [CrossRef]
22. Nordt, L.C.; Driese, S.G. A modern soil characterization approach to reconstructing physical and chemical properties of paleo-Vertisols. *Am. J. Sci.* **2010**, *310*, 37–64. [CrossRef]
23. Stinchcomb, G.E.; Nordt, L.C.; Driese, S.G.; Lukens, W.E.; Williamson, F.C.; Tubbs, J.D. A data-driven spline model designed to predict paleoclimate using paleosol geochemistry. *Am. J. Sci.* **2016**, *316*, 746–777. [CrossRef]
24. Knott, S.D. The Liguride complex of southern Italy—A Cretaceous to Paleogene accretionary wedge. *Tectonophysics* **1987**, *142*, 217–226. [CrossRef]
25. Monaco, C.; Tortorici, L. Tectonic role of ophiolite-bearing terranes in the development of the Southern Apennines orogenic belt. *Terra Nova* **1995**, *7*, 153–160. [CrossRef]
26. Pescatore, T.; Renda, P.; Schiattarella, M.; Tramutoli, M. Stratigraphic and structural relationships between Meso-Cenozoic Lagonegro basin and coeval carbonate platforms in southern Apennines, Italy. *Tectonophysics* **1999**, *315*, 269–286. [CrossRef]
27. Ogniben, L. Schema introduttiva alla geologia del confine Calabro-Lucano. *Mem. Soc. Geol. Ital.* **1969**, *8*, 453–763.
28. Mostardini, F.; Merlini, S. Appennino Centro. Meridionale e Proposta di Modello Strutturale. *Mem. Soc. Geol. Ital.* **1986**, *35*, 177–202.
29. Pescatore, T.; Renda, P.; Tramutoli, M. Relationship between the Lagonegro and Silicidi formations of the middle valley of the Basento River, Lucca, Southern Apennines. *Mem. Soc. Geol. Ital.* **1988**, *41*, 353–361.
30. Marsella, E.; Bally, A.W.; D'Argenio, B.; Cippitelli, G.; Pappone, G. Tectonic history of the Lagonegro Domain and Southern Apennine thrust belt evolution. *Tectonophysics* **1995**, *252*, 307–330. [CrossRef]
31. Fiore, S.; Piccarreta, G.; Santaloia, F.; Santarcangelo, R.; Tateo, F. The Flysch Rosso shales from the southern Apennines, Italy. 1. Mineralogy and geochemistry. *Per. Mineral.* **2000**, *69*, 63–68.
32. Mongelli, G. Trace elements distribution and mineralogical composition in the <2-μm size fraction of shales from the Southern Apennines, Italy. *Mineral. Petrol.* **1995**, *53*, 103–114.
33. Caggianelli, A.; Fiore, S.; Mongelli, G.; Salvemini, A. REE distribution in the clay fraction of pelites from the southern Apennines, Italy. *Chem. Geol.* **1992**, *99*, 253–263. [CrossRef]
34. Franzini, M.; Leoni, L.; Saitta, M. A simple method to evaluate the matrix effects in X-ray fluorescence analysis. *X-ray Spectrom.* **1972**, *1*, 151–154. [CrossRef]
35. Franzini, M.; Leoni, L.; Saitta, M. Revisione di una metodologia analitica per fluorescenza-X, basata sulla correzione completa degli effetti di matrice Rend. *Soc. Ital. Mineral. Petrol.* **1975**, *31*, 365–378.
36. Leoni, L.; Saitta, M. Determination of yttrium and niobium on standard silicate rocks by X-ray fluorescence analyses Rend. *Soc. Ital. Mineral. Petrol.* **1976**, *32*, 497–510.
37. Govindaraju, K.; Mevelle, G. Fully automated dissolution and separation methods for inductively coupled plasma atomic emission spectrometry rock analysis. Application to the determination of rare earth elements. Plenary lecture. *J. Anal. Atom. Spectrom.* **1987**, *2*, 615–621.
38. Mongelli, G. Ce-anomalies in the textural components of Upper Cretaceous karst bauxites from the Apulian carbonate platform (southern Italy). *Chem. Geol.* **1997**, *140*, 69–79. [CrossRef]
39. Herron, M.M. Mineralogy from geochemical well logging. *J. Sedim. Petrol.* **1986**, *58*, 820–829. [CrossRef]
40. Fiore, S.; Mongelli, G. Hypothesis on the genesis of day minerals in the fine fraction of «Argille varicolori» from Andretta (southem Apennines). *Miner. Petrog. Acta* **1991**, *34*, 183–190.
41. Di Leo, P.; Dinelli, E.; Mongelli, G.; Schiattarella, M. Geology and geochemistry of Jurassic pelagic sediments, Scisti silicei Formation, southern Apennines. *Italy Sed. Geol.* **2002**, *150*, 229–246. [CrossRef]
42. Mongelli, G.; Dinelli, E. The geochemistry of shales from the "Frido Unit", Liguride Complex, Lucanian Apennines, Italy: Implications for provenance and tectonic setting. *Ofiotiti* **2001**, *26*, 457–466.
43. Davis, J.C. *Statistics and Data Analysis in Geology*; John Wiley & Sons: New York, NY, USA, 1986.
44. Ahmadnejad, F.; Mongelli, G. Geology, geochemistry, and genesis of REY minerals of the late Cretaceous karst bauxite deposits, Zagros Simply Folded Belt, SW Iran: Constraints on the ore-forming process. *J. Geochem. Explor.* **2022**, *240*, 107030. [CrossRef]
45. Ferhaoui, S.; Kechiched, R.; Bruguier, O.; Sinisi, R.; Kocsis, L.; Mongelli, G.; Bosch, D.; Ameur Zaimeche, O.; Laouar, R. Rare earth elements plus yttrium (REY) in phosphorites from the Tébessa region (Eastern Algeria): Abundance, geochemical distribution through grain size fractions, and economic significance. *J. Geochem. Explor.* **2022**, *241*, 107058. [CrossRef]
46. Liu, Y.H.; Lee, D.C.; You, C.F.; Takahata, N.; Iizuka, Y.; Sano, Y.; Zhou, C. In-situ U–Pb dating of monazite, xenotime, and zircon from the Lantian black shales: Time constraints on provenances, deposition and fluid flow events. *Precambrian Res.* **2020**, *349*, 105528. [CrossRef]

47. Perri, F.; Critelli, S.; Martín-Martín, M.; Montone, S.; Amendola, U. Unravelling hinterland and offshore palaeogeography from pre-to-syn-orogenic clastic sequences of the Betic Cordillera (Sierra Espuña), Spain. *Palaeogeogr. Palaeoclimatol. Palaeoecol.* **2017**, *468*, 52–69. [CrossRef]
48. Abedini, A.; Mongelli, G.; Khosravi, M.; Sinisi, R. Geochemistry and secular trends in the middle–late Permian karst bauxite deposits, northwestern Iran. *Ore Geol. Rev.* **2020**, *124*, 103660. [CrossRef]
49. Michel, L.A.; Sheldon, N.D.; Myers, T.S.; Tabor, N.J. Assessment of pretreatment methods on CIA-K and CALMAG indices and the effects on paleoprecipitation estimates. *Palaeogeogr. Palaeoclimatol. Palaeoecol.* **2022**, *601*, 111102. [CrossRef]
50. Maynard, J.B. Chemistry of modern soils as a guide to interpreting Precambrian paleosols. *J. Geol.* **1992**, *100*, 279–289. [CrossRef]
51. Viers, J.; Wasserburg, G.J. Behavior of Sm and Nd in a lateritic soil profile. *Geochim. Et Cosmochim. Acta* **2004**, *68*, 2043–2054. [CrossRef]
52. Condie, K.C. Chemical composition and evolution of the upper continental crust: Contrasting results from surface samples and shales. *Chem. Geol.* **1993**, *104*, 1–37. [CrossRef]
53. McLennan, S.M.; Taylor, S.R. Sedimentary rocks, and crustal evolution: Tectonic setting and secular trends. *J. Geol.* **1991**, *99*, 1–21. [CrossRef]